Research in Astronomy and Astrophysics, 24:125018 (15pp), 2024 December https://doi.org/10.1088/1674-4527/ad8ead

Simulating the Peculiar Periphery of the Cygnus Loop

Jun-Yu Shen[1], Bi-Wen Bao[1,2], and Li Zhang[1]
[1] Department of Astronomy, Key Laboratory of Astroparticle Physics of Yunnan Province, Yunnan University, Kunming 650091, China; baobiwen@ynu.edu.cn, lizhang@ynu.edu.cn
[2] Key Laboratory of Statistical Modeling and Data Analysis of Yunnan Province, Yunnan University, Kunming 650091, China
Received 2024 September 7; revised 2024 October 18; accepted 2024 November 1; published 2024 December 9

Abstract

The middle-aged Galactic supernova remnant (SNR)- the Cygnus Loop (CL)- displays a peculiar morphology in X-rays, featuring a blowout in the southern region. The underlying process accounting for the formation of the peculiar periphery remains a mystery. To this end, we conduct hydrodynamical simulations to investigate the SNR evolution coupled with a tailored stellar-wind model: a bipolar stellar wind emanating from a runaway red supergiant progenitor, excavating a wind-blown cavity elongated along the $-z$-direction. Our simulation results reveal that the forward shock of the consequent SNR sweeps up the modified ambient media, shaping the overall morphology with a blowout comparable to that of CL. Besides, a series of simulation runs are performed to assess the impacts of different model parameters and the projection effect (observational angle $\theta_{\rm obs}$) on the final SNR profile. Three physical quantities are extracted from simulation results to characterize the simulated SNR and make a direct comparison with the X-ray observations of CL. We find that the final SNR morphology is sensitive to both stellar-wind properties and $\theta_{\rm obs}$. A Cygnus-Loop-like SNR could be reproduced under appropriate parameter combinations at $\theta_{\rm obs} = 0^\circ$. While for $\theta_{\rm obs} \lesssim 30^\circ$, the projected morphology akin to CL could be also generated under specific conditions.

Key words: hydrodynamics – methods: numerical – ISM: supernova remnants

1. Introduction

The Cygnus Loop (G74.0-8.5) is a Galactic supernova remnant (SNR) with an age of ~ 1.0–2.5×10^4 yr (E. Miyata et al. 1994; N. A. Levenson et al. 1998; H. Uchida et al. 2008; J. Y. Seok et al. 2020). Based on Gaia EDR3 parallaxes, the diameter of the Cygnus Loop is ~ 37 pc from east to west determined by an estimated distance of $\sim 725 \pm 25$ pc (R. A. Fesen et al. 2018b, 2021). Considering the existing observational evidence, it is generally believed that the explosive energy is subenergetic ($\lesssim 1.0 \times 10^{51}$ erg) (S. Rappaport et al. 1974; E. Miyata & H. Tsunemi 1999; A. Preite Martinez 2011; R. A. Fesen et al. 2018b). This specific source is supposed to be a core-collapse SNR with the total mass of the ejecta being $\sim 4.1\,M_\odot$ (E. Miyata et al. 1998; R. A. Fesen et al. 2018a), and the main-sequence mass for the progenitor is estimated to be $\sim 15\,M_\odot$ (E. Miyata & H. Tsunemi 1999), indicating a red supergiant (RSG; V. V. Dwarkadas 2005; E. M. Levesque 2010).

The morphology of the Cygnus Loop seen in X-rays is nearly circular with a clear breakout to the south (see Figure 1) (F. D. Seward 1990; N. A. Levenson et al. 1997, 1999). Concerning such a peculiar periphery, there exist divergent viewpoints: some authors have questioned whether this source consists of two separate SNRs, citing disparities in radio morphology and polarization intensity between the dominant region and the southern blowout (B. Uyanıker 2002; X. H. Sun et al. 2006). However, more observational evidence implies that this source is one single SNR: (1) the smooth profiles of the X-ray and radio emission from its northern part to the southern blowout (B. Aschenbach & D. A. Leahy 1999); (2) the existence of similarities in plasma temperature and the abundances of elements between the northern and southern region (H. Uchida et al. 2008); and (3) the resemblance of spectra between the southern and northern regions from temperature versus temperature plots (X. H. Sun et al. 2022). The above-mentioned similarities would be disrupted by discontinuities in the contacting region if this source involves two separate SNRs (H. Uchida et al. 2008; R. A. Fesen et al. 2018b).

Assuming that the Cygnus Loop is indeed one single SNR, then an appropriate interpretation is required for the formation of the observed southern blowout. Since SNRs are the results of interactions between the expanding ejecta and the surrounding interstellar medium (ISM), peculiar morphological features, as observed in SNRs such as Kepler (G. Cassam-Chenaï et al. 2004; S. P. Reynolds et al. 2007), RCW 86 (B. J. Williams et al. 2011) and IC 443 (K.-J. Lee et al. 2012), are presumably related with the structure and composition of both ejecta and the surrounding ISM. Concerning the Cygnus Loop's peculiar morphology, particular attention has been devoted to seeking its physical origin, and two hypotheses have been proposed in

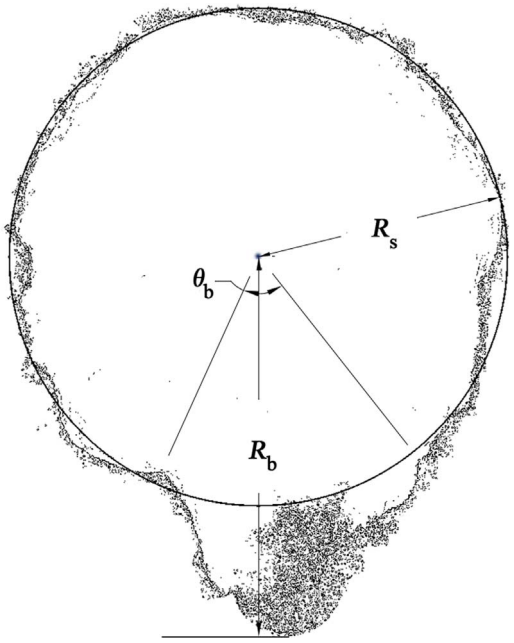

Figure 1. Schematic diagram for the X-ray morphology of the Cygnus Loop: the periphery of the shaded area represents the limb of the Cygnus Loop in X-rays with ROSAT High Resolution Imager observations (N. A. Levenson et al. 1998, 1999). The original picture is downloaded from http://imagine.gsfc.nasa.gov/Images/rosat/snr_cygloop.html. Excluding the southern blowout, we match the general limb of the northern part with a circle, with the center of this circle marking the northern geometric center. Three physical quantities (the central angle of the blowout θ_b, the average radius of the northern circular limb R_s, and the distance from the center of the circle to the southernmost point of the contour R_b) are extracted to characterize the Cygnus Loop.

the literature: (1) several studies suggest that the morphology of the Cygnus Loop could be attributed to the evolution of ejecta in a preexisting cavity produced by the progenitor system (R. McCray & T. P. J. Snow 1979; J. J. Hester & D. P. Cox 1986; N. A. Levenson et al. 1997; H. Uchida et al. 2009), where the southern blowout is inferred as the product of SNR-cavity interactions. Such a cavity is speculated to be low-density and wind-driven, with a high-density shell bordering the ISM (P. A. Charles et al. 1985; R. Braun & R. G. Strom 1986; E. Miyata & H. Tsunemi 1999). Meanwhile, the optical observations suggest that the Cygnus Loop processes a systemic velocity assessed to be $\sim$30 km s^{-1} in the local standard of rest (R. Minkowski 1958; R. P. Kirshner & K. Taylor 1976; P. Shull & H. Hippelein 1991), which could leave imprints on the formation of the cavity. Based on these findings, several numerical works utilize the SNR-cavity interaction model and reproduce the Cygnus Loop's peculiar morphology (D. M.-A. Meyer et al. 2015; J. Fang et al. 2017; D. M.-A. Meyer et al. 2020, 2024); (2) another hypothesis interprets the peculiar morphology as the consequence of an SNR expanding in an extended low-density region surrounded by molecular clouds with different densities (P. A. Charles et al. 1985; R. A. Fesen et al. 2018b). For both hypotheses, the appearance of the blowout is due to the SNR's forward shock (FS) traveling into a low-density tunnel of $\sim$10 pc in width (W. H.-M. Ku et al. 1984; B. Aschenbach & D. A. Leahy 1999; H. Uchida et al. 2009).

D. M.-A. Meyer et al. (2015) conducted general research on the origin of Galactic asymmetric SNRs and proposed an ejecta-wind interaction model. Specifically, if a massive star moves supersonically through the ISM, a bow shock will emerge with a low-density region trailing behind it (R. Bandiera 1987). When the supernova (SN) explosion occurs, the blast wave collides with the stellar wind and the bow shock, forming a spherical morphology in one direction. While in the opposite direction, the blast wave encounters less resistance due to traveling in the low-density region, generating an asymmetric remnant. Motivated by D. M.-A. Meyer et al. (2015), J. Fang et al. (2017) reproduced the morphology of the Cygnus Loop with 3D numerical simulations by assuming a runaway progenitor star, which evacuates a cavity through two-stage anisotropic and latitude-dependent stellar winds with varying speeds and durations. Then, a core-collapse SN explodes, whose FS interacts with the cavity and then forms the drop-like morphology. Recent studies by D. M.-A. Meyer et al. (2020, 2024) demonstrated that the motion of a massive progenitor star, accompanied by time-dependent stellar winds, could also engender Cygnus-Loop-like SNRs. The specific SNR morphology could be attained through an SN explosion within either an elongated or a drop-like cavity, which results from the time-dependent stellar winds.

Despite ongoing debate, the question of whether the formation of the Cygnus Loop's peculiar morphology is solely attributed to stellar winds or influenced by other factors remains controversial. The stellar-wind model discussed above offers a plausible explanation for the formation of the Cygnus Loop, particularly the southern blowout (R. A. Fesen et al. 2018a). However, due to the unclear mechanism of the stellar wind, there is room for further research to assess alternative assumptions, regarding the formation of the preexisting cavity as well as the blowout. Such investigations could offer valuable insights into the origin of this distinctive morphology.

In this paper, utilizing hydrodynamical (HD) simulations, we try to explain the unique profile of the Cygnus Loop SNR. Considering that the progenitor of the Cygnus Loop may be an RSG, we propose one possible scenario: the progenitor star possesses a spatial velocity directed toward the $+z$-direction, while the spatial distribution of its stellar wind is bipolar-like, which varies with respect to the angle from the $+z$-direction.

This paper is structured in the following manners. In Section 2, we construct our numerical models for the stellar wind and a core-collapse SNR. In Section 3, we present the simulation results for the formation of the Cygnus Loop. We provide a discussion and summarize the main results in Section 4.

2. Model Descriptions

2.1. Numerical Methods

This section introduces numerical models for the stellar wind of the progenitor and the numerical setups for a core-collapse SNR within the wind-blown cavity. The PLUTO code (Mignone et al. 2007; A. Mignone et al. 2012) is used to perform the HD numerical simulations. The Euler equations are used to study the dynamical properties:

$$\frac{\partial \rho}{\partial t} + \nabla \cdot (\rho \boldsymbol{u}) = 0; \tag{1}$$

$$\frac{\partial \rho \boldsymbol{u}}{\partial t} + \nabla \cdot (\rho \boldsymbol{u}\boldsymbol{u}) + \nabla P = 0; \tag{2}$$

$$\frac{\partial E}{\partial t} + \nabla \cdot [(E + P)\boldsymbol{u}] = 0, \tag{3}$$

where t, $\boldsymbol{u}$, P, are the time, velocity, and thermal pressure, respectively. The total energy density E is

$$E = \frac{1}{2}\rho u^2 + \rho\varepsilon. \tag{4}$$

The mass density is $\rho = \mu \mathrm{m_H} n$, and the mass of the hydrogen atom is $m_{\rm H}$. The mean molecular weight of the ionized gas is $\mu = 0.6$ with a H:He ratio of $10:1$. n is the gas number density and ε is the internal energy density. Throughout this manuscript, the mass density is in units of $m_{\rm H}\,\mathrm{cm}^{-3}$, and all other physical quantities are expressed in c.g.s units.

Equations (1)–(4) are numerically solved using a second-order Runge–Kutta method, coupled with the Harten–Lax–Van Leer approximate Riemann Solver incorporating the middle contact discontinuity (HLLC) and finite volume methodology.

2.2. Constructing the Stellar-wind Model

Planetary nebulae (PNe) are the circumstellar gas ejected from the central star during an intense mass-losing phase (O. De Marco 2009), characterized by symmetrical morphologies (B. Balick & A. Frank 2002). In the past few decades, bipolar PNe are frequently observed in the vicinity of RSGs (P. Hekkert et al. 1992; W. Brandner et al. 1997; B. Davies et al. 2007; S. Muller 2007), and such peculiar PNe are widely considered as the outcomes of the bipolar stellar winds. Meanwhile, the formation of bipolar stellar winds could be attributed to various physical mechanisms, such as rapid stellar rotation (S. M. Asida & Y. Tuchman 1995; G. García-Segura & J. A. López 2000), magnetic tension (G. García-Segura 1997; G. García-Segura et al. 2005), and asymmetric thermal conduction (S. A. Zhekov & A. V. Myasnikov 2000). Given that a large proportion of core-collapse SNRs might originate from the explosion of RSGs (V. V. Dwarkadas 2005; S. Katsuda et al. 2018), some numerical simulation studies have been carried out to investigate the influences of the bipolar-like winds generated by RSGs on the morphology of subsequent SNRs (J. M. Blondin & P. Lundqvist 1993; J. M. Blondin et al. 1996; V. V. Dwarkadas et al. 1996; P. F. Velázquez et al. 2023).

Our simulations, encompassing the evolution of both the stellar wind and the SNR, are conducted in a cylindrical coordinate system. A uniform grid of 2048×4096 grid cells is mapped onto a domain of size $[0, 20] \times [-36, 16]\,\mathrm{pc}^2$ in the (r, z) plane (r and z are the abscissa and ordinate in a cylindrical coordinate system, respectively). In this section, we consider a bipolar stellar wind for the progenitor star with a constant spatial velocity $v_\star$ directed toward the $+z$-direction. The stellar-wind density $\rho_{\rm wind}$ is written as:

$$\rho_{\rm wind} = \frac{\dot{M}}{4\pi r_\star^2 u_{\rm wind}}, \tag{5}$$

where $\dot{M}$, $r_\star$, and $u_{\rm wind}$ are the mass-loss rate, the radius from the progenitor, and the stellar-wind velocity, respectively (A. Chiotellis et al. 2012; S. Das et al. 2022). Following Equation (1) in A. Chiotellis et al. (2020), $u_{\rm wind}$ is expressed as:

$$u_{\rm wind} = u_0[1 - \alpha|\sin\theta|^k]. \tag{6}$$

Here, θ is the angle from the $+z$-direction. u_0 is the stellar-wind velocity at $\theta = 0°$ and $180°$ (i.e., $r = 0$). α and k are constants. Therefore, the stellar-wind velocity is higher at $r = 0$ and lower when $\theta = 90°$ ($z = 0$) (see Figure 2 in A. Chiotellis et al. 2020). After the stellar-wind evolution, we adopt the density, pressure, and velocity distributions of the wind-blown structures as the initial physical conditions of the ambient media for the evolution of SNR.

More specifically, we fix the spatial velocity $v_\star = 30\,\mathrm{km\,s}^{-1}$ for the progenitor star, according to the observations (R. Minkowski 1958; R. P. Kirshner & K. Taylor 1976; P. Shull & H. Hippelein 1991). Assuming a wind temperature of $T_{\rm wind} = 3.2 \times 10^3\,\mathrm{K}$ (D. M.-A. Meyer et al. 2015), a wind velocity of $u_0 = 200\,\mathrm{km\,s}^{-1}$ at $r = 0$ (P. Massey & K. A. G. Olsen 2003; E. R. Beasor et al. 2020), and a mass-loss rate of $\dot{M} = 1 \times 10^{-6}\,M_\odot\,\mathrm{yr}^{-1}$ (B. Davies 2017; E. R. Beasor et al. 2020; D. M.-A. Meyer et al. 2021a), the wind is simulated as material continuously injected from a boundary with a radius of 0.5 pc. While we adopt $T_0 = 10^4\,\mathrm{K}$ for the background temperature (N. A. Levenson et al. 1999) and $n_{\rm ISM} = 0.16\,\mathrm{cm}^{-3}$ for the number density of ISM (W. H.-M. Ku et al. 1984; N. A. Levenson et al. 1998; J. Bohigas et al. 1999). α and k are taken to be 0.9 and 3.0, respectively (A. Chiotellis et al. 2020).

2.3. Initial Density Profiles of a Core-collapse SNR

We use the power-law profile to describe the mass density structure of the ejecta, containing a kinetic energy of $E_{\rm ej}$ and a mass of $M_{\rm ej}$. The density profile is truncated at $r_{\rm c} = v_{\rm c}t$, beyond which the density of the ejecta follows a power-law and the mass of the ejecta accounts for $3/7$ of the total mass. Whereas a

constant density is assumed in the region within r_c, where the ejecta mass is 4/7 of the total mass (R. Chevalier 1982; J. M. Blondin & D. C. Ellison 2001):

$$\rho_{ej}(r, t) = \begin{cases} \rho_c v_c^s r^{-s} t^{s-3} & \text{for } r > v_c t, \\ \rho_c t^{-3} & \text{for } r < v_c t, \end{cases} \quad (7)$$

where t is the age since the SN explosion, and the power-law index $s = 9$ is for core-collapse SNRs. The constant ρ_c is:

$$\rho_c = \frac{5\,s - 25}{2\pi s} E_{ej} v_c^{-5}, \quad (8)$$

and v_c can be determined as follows:

$$v_c = \left(\frac{10\,s - 50}{3\,s - 9} \frac{E_{ej}}{M_{ej}} \right)^{1/2}, \quad (9)$$

In our simulations, the parameters for initialization of the core-collapse SNR are set to $E_{ej} = 0.06 \times 10^{51}$ erg (A. Preite Martinez 2011; R. A. Fesen et al. 2018b), $M_{ej} = 5.0\,M_\odot$ (J. Fang et al. 2017), and the initial radius of the ejecta $R_{ej} = 0.27$ pc (corresponding to an initial age of about 60 yr) (R. Chevalier 1982; J. M. Blondin & D. C. Ellison 2001).

The system is in the rest frame of the progenitor, namely that the ISM with a spatial velocity $v_\star$ acts as an inflow parallel to the $-z$-direction. The stellar wind is injected from a sphere (0.5 pc in radius) with a mass-loss rate of $\dot{M}$, a θ-dependent velocity of u_{wind}, and a duration of t_{wind}. The total integration time for stellar wind t_{wind} is selected as 400 kyr (P. F. Velázquez et al. 2023). Then, a core-collapse SNR is introduced at the coordinate origin, whose age in the simulations is defined as t_{SNR}. Given that the evaluated age of the Cygnus Loop is about 1.0–2.5 $\times 10^4$ yr (E. Miyata et al. 1994; N. A. Levenson et al. 1998; H. Uchida et al. 2008; J. Y. Seok et al. 2020), we follow the remnant evolution for $t_{SNR} = 22.0$ kyr in our simulations.

2.4. Projection of Simulated SNRs at Different Observational Angles

It should be noted that Figure 1 is the projection of the Cygnus Loop along the direction perpendicular to the line of sight in soft X-rays. In fact, the direction of propagation of the runaway star may not be absolutely perpendicular to the line of sight. The same projected morphology of the Cygnus Loop may be reproduced with various combinations of mass-loss rate, stellar-wind velocity, and stellar-wind integration time, depending on the orientation of the remnant relative to the line of sight. For instance, assuming an inclination of the remnant's symmetry axis less than 90°, a higher mass-loss rate or wind velocity, and even a longer stellar-wind integration time, could produce the same projected morphology. In light of this, the values of physical quantities extracted from Figure 1 may not reflect the real situation, if the angle seriously deviates from 90°.

As an attempt to study the projected morphology of an SNR at any observational angle θ_{obs} (the viewing angle to the equatorial plane, namely the x–y plane at $z = 0$ D. M.-A. Meyer et al. 2021b), we conduct a series of new simulations with a $[-20, 20] \times [-20, 20] \times [-36, 16]$ pc^3 computational domain in a Cartesian coordinate system, which is mapped with a uniform grid made of $512 \times 512 \times 512$ grid zones. With analogous initial setups as in Sections 2.2 and 2.3, the projected patterns of SNRs will be performed in the 3D Cartesian coordinate system.[3] More explicitly, we generate the projected maps of the square of the SNR density in each model, which roughly approximates the intensity of thermal X-ray emission along a given line of sight with θ_{obs} (G. Ferrand et al. 2010). The intensity in our projected maps is calculated as:

$$I = \frac{\int \rho^2(\theta_{obs}) dl}{\int dl}, \quad (10)$$

with $\rho(\theta_{obs})$ the observed density of SNR for an observational angle of θ_{obs} and l the depth along line of sight.

3. Results

In this section, HD simulations are employed to replicate the unique X-ray morphology of the Cygnus Loop, based on the scenario presented in Section 2.2. Since we do not include magnetic fields in the simulation runs, the resulting SNR's density profile is utilized to represent its X-ray image. We extract the outline of the Cygnus Loop in X-rays in Figure 1. Excluding the southern blowout, we match the general limb of the northern part with a circle, with the center of this circle marking the northern geometric center (N. A. Levenson et al. 1998). In order to characterize the Cygnus Loop in geometry, we define three physical quantities in Figure 1: the distance from the northern center to the southernmost point of the contour R_b, the average radius of the northern circular limb R_s, and the central angle of the blowout θ_b. In the following discussion, we intend to extract these three physical quantities from our resulting SNRs to facilitate a comprehensive comparison between our resulting SNRs and the Cygnus Loop,[4] thus properly assessing the proposed stellar-wind model. Table 1 lists seven models with different stellar-wind properties, which are referred to as Model A–D_2. We take Model A as the benchmark case.

3.1. Stellar-wind Evolution for Model A

Figure 2 illustrates the evolution of density maps for the stellar wind in Model A. On account of the supersonic

[3] For 3D simulations, we adopt an initial radius of 0.64 pc (corresponding to an initial SNR age ~160 yr) to better describe the initial density distribution (R. Chevalier 1982; J. M. Blondin & D. C. Ellison 2001).

[4] The three extracted physical quantities are independent of the distance to the Cygnus Loop.

Table 1
Parameters for our RSG stellar-wind model with the others $T_0 = 10^4$ K, $n_{\rm ISM} = 0.16$ cm^{-3}, $T_{\rm wind} = 3.2 \times 10^3$ K, $v_\star = 30$ km s^{-1}, $\alpha = 0.9$, $k = 3.0$, $M_{\rm ej} = 5.0\,M_\odot$, $E_{\rm ej} = 0.06 \times 10^{51}$ erg, $t_{\rm SNR} = 22.0$ kyr. The bold values in the table highlight the parameters that have been altered in each model, with respect to Model A, while other parameters remain unchanged.

Models Comparison Properties				
(1)	(2)	(3)	(4)	(5)
Model Name	Parameter Changed	$\dot{M}$ ($M_\odot$ yr^{-1})	u_0 (km s^{-1})	$t_{\rm wind}$ (kyr)
A	···	1×10^{-6}	200	400
B_1	Stellar-wind mass-loss rate	$\mathbf{5 \times 10^{-6}}$	200	400
B_2	Stellar-wind mass-loss rate	$\mathbf{1 \times 10^{-5}}$	200	400
C_1	Stellar-wind velocity	1×10^{-6}	**80**	400
C_2	Stellar-wind velocity	1×10^{-6}	**400**	400
D_1	Stellar-wind integration time	1×10^{-6}	200	**600**
D_2	Stellar-wind integration time	1×10^{-6}	200	**800**

propagation of the wind into the ISM, a two-shock structure (i.e., the "wind-blown bubble" J. Castor et al. 1975; R. Weaver et al. 1977; S. Das et al. 2022) appears around the progenitor star. As required by Equation (6), the wind bubble initially manifests itself in a bipolar-like shape ($t_{\rm wind} = 60$ kyr). Meanwhile, a low-density cavity emerges within the reverse shock (RS) of the wind. During the stellar-wind evolution, owing to the proper motion of the progenitor, an interaction occurs between the stellar wind and the inflowing ISM. Therefore, the bubble is elongated along the $-z$-direction with the wind injection, deviating from its bipolar-like shape. As a consequence, the low-density cavity extends more rapidly in the south. Furthermore, due to the high stellar-wind velocity ($u_0 = 200$ km s^{-1}) for a $\theta \gtrsim 150°$, a large pressure difference between the two sides of the contact discontinuity (CD) could be yielded. This contributes to the development of some instability structures at the CD (B.-I. Jun & T. W. Jones 1999). At $t_{\rm wind} = 400$ kyr, the bottom of the cavity is close to the mark of $z = -18$ pc, and a southern low-density tunnel is formed. These remaining stellar-wind structures will serve as the initial background for the subsequent SN explosion.

3.2. SNR Evolution for Model A

We adopt the density, pressure, and velocity of the wind-blown structures as the initial background conditions for a subsequent core-collapse SNR. The SN ejecta is introduced at the origin of coordinates, as illustrated in Figure 3. Since the SN explosion, an FS and an RS are formed due to the supersonic movement of the ejecta, as revealed at $t_{\rm SNR} = 2.0$ kyr. The CD is located between the shocked ambient medium and the shocked ejecta, where some finger-like structures gradually appear and affect the morphology of the FS because of the Rayleigh–Taylor instabilities (RTI; Y. Zhou 2017a, 2017b).

Initially, the FS interacts with the free stellar wind and sweeps the shocked wind as well as the shocked ISM. Then, because of the collisions with the remaining wind structures, the profile of the FS demonstrates a deviation from sphericity. After that, the northern part of the FS moves into the uniform ambient medium. In the opposite direction, the southern part propagates within the low-density cavity, leading to a protrusion. When $t_{\rm SNR}$ is 22.0 kyr, the evident protrusion resembles the observed blowout of the Cygnus Loop. For better comparisons with the results of X-ray observations, we perform mirror symmetry on the image of the simulated remnant at $t_{\rm SNR} = 22.0$ kyr to synthesize the bottom image in Figure 3. The simulated SNR displays a generally circular outline with a distinct southern protrusion, analogous to the observations.

3.3. Comparison of Different Models in Table 1

In this section, we evaluate the influences engendered by the stellar wind of the progenitor in the morphological properties of final SNRs, especially the southern blowouts. Considering that the final profile of SNR is determined by the combination of the SNR and stellar-wind characteristics (G. Tenorio-Tagle et al. 1990, 1991; J. Vink 2012), there exists a vast parameter space in our modeling. Here, we mainly focus on the stellar-wind properties and set up seven different models in Table 1. Specifically, the parametric space we study is centered on Model A, and the other six models are produced by varying $\dot{M}$, $u_{\rm wind}$, and $t_{\rm wind}$, respectively (A. Chiotellis et al. 2020).

The panels in Figure 4 portray the density maps of the stellar wind for Models B_1–D_2 in Table 1, while the panels of Figure 5 are for their subsequent SNR's density profiles, respectively. The primary conclusions obtained from our simulations are as follows:

Varying the mass-loss rate. Owing to the high mass-loss rate of the stellar wind in Models B_1 ($\dot{M} = 5 \times 10^{-6}\,M_\odot$ yr^{-1}) and B_2 ($\dot{M} = 10^{-5}\,M_\odot$ yr^{-1}), the low-density cavity excavated by the stellar wind expands further, displaying a roughly bipolar-like shape at $t_{\rm wind} = 400$ kyr. As a result, within the timescale of our simulations, the final SNR morphology deviates from the Cygnus-Loop-like shape in Model A.

Varying the wind velocity. With a low u_0 of 80 km s^{-1} (Model C_1), the stellar wind creates a smaller cavity around the progenitor system compared with that in Model A. Since there is a scarcity of low-density areas in the south for the FS to

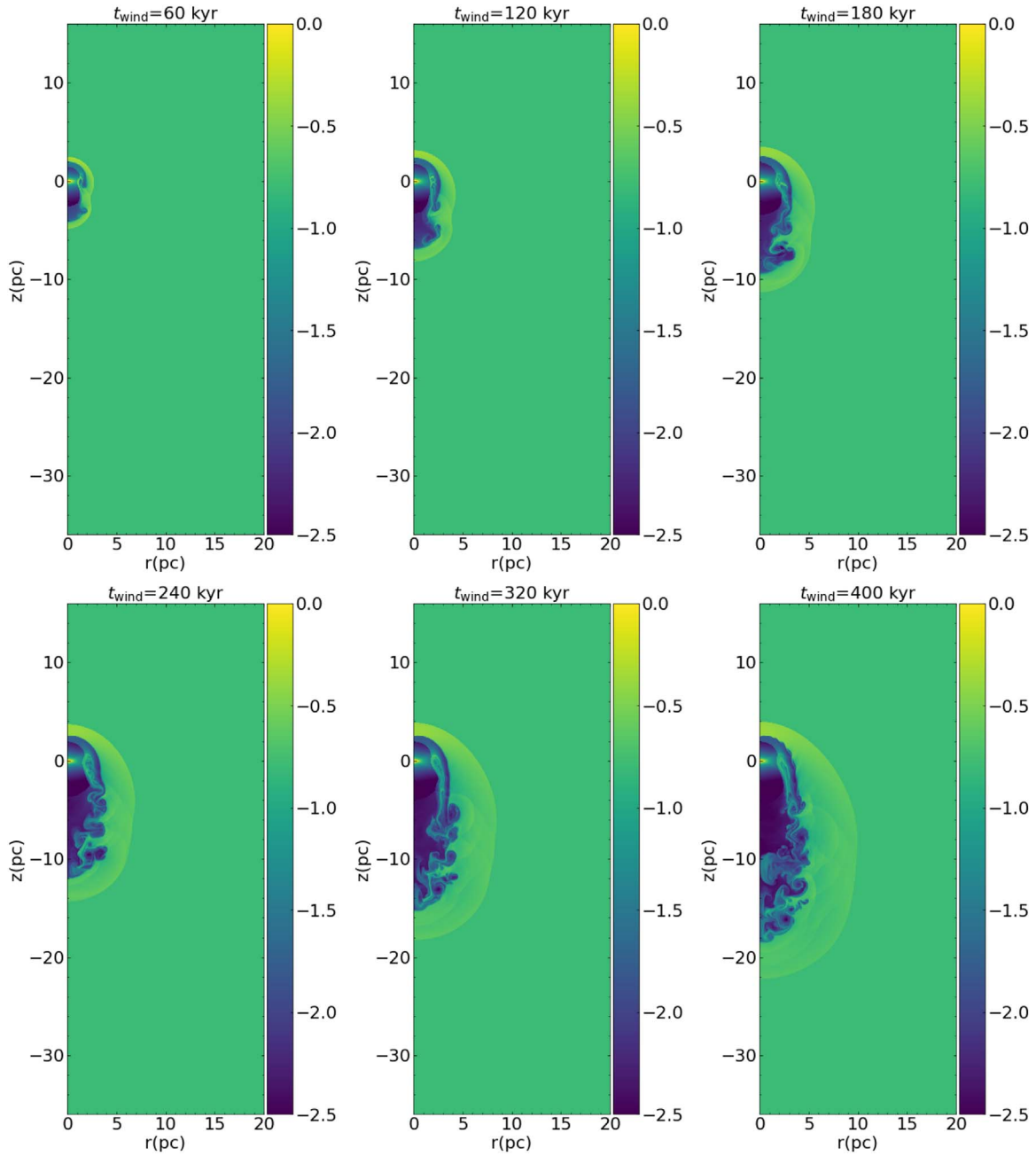

Figure 2. Density maps of the stellar wind for Model A at different times. $t_{\rm wind}$ is the time for stellar-wind evolution. The color bars show the logarithm of density in units of $m_{\rm H}\,{\rm cm}^{-3}$.

travel freely, the interactions between the subsequent SNR and those circumstellar structures could not result in a manifested blowout. In contrast, a high u_0 of 400 km s^{-1} (Model C_2) leads to a further expansion of the cavity in both the $-z$ and r-direction. This enables the FS inside the southern cavity to traverse a longer distance in both directions during the simulation time, thus giving rise to an excessively large blowout at $t_{\rm SNR} = 22$ kyr.

Varying the integration time for the stellar wind. In Models D_1 ($t_{\rm wind} = 600$ kyr) and D_2 ($t_{\rm wind} = 800$ kyr), a long integration time engenders the elongation of the cavity along the $-z$-direction, as well as some alterations in the boundary structures of the southern cavity. Consequently, the northern part of the resulting SNRs resemble that in Model A. In the southern cavity, the FS covers a larger distance along the $-z$-direction at $t_{\rm SNR} = 22$ kyr, producing a stretched blowout.

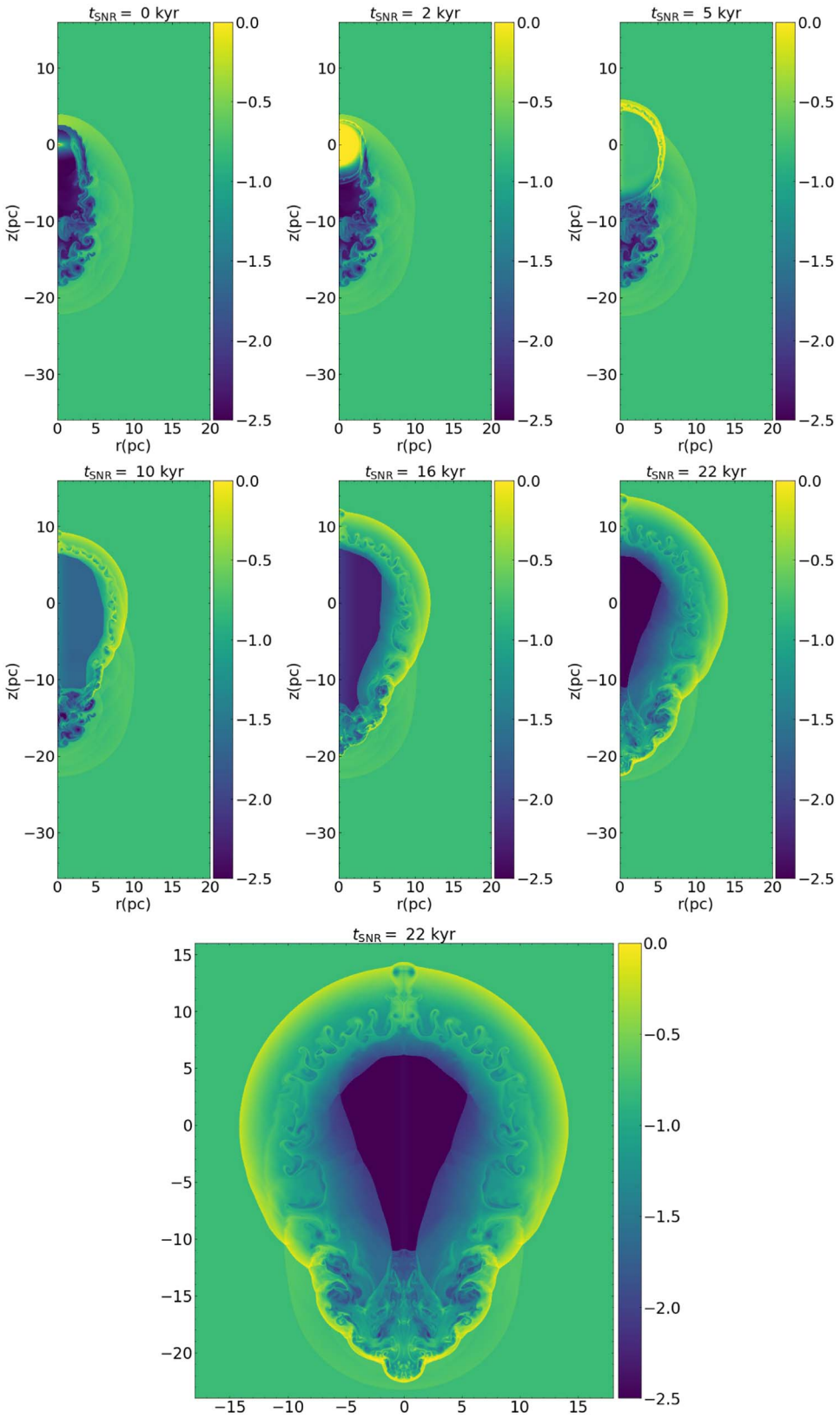

Figure 3. The upper six panels: density profiles of the SNR for Model A at different times (shown on a logarithmic scale in units of $m_{\rm H}\,{\rm cm}^{-3}$). The bottom panel: synthesized image of the density profile of the SNR at $t_{\rm SNR} = 22.0$ kyr, where $t_{\rm SNR}$ is the SNR age.

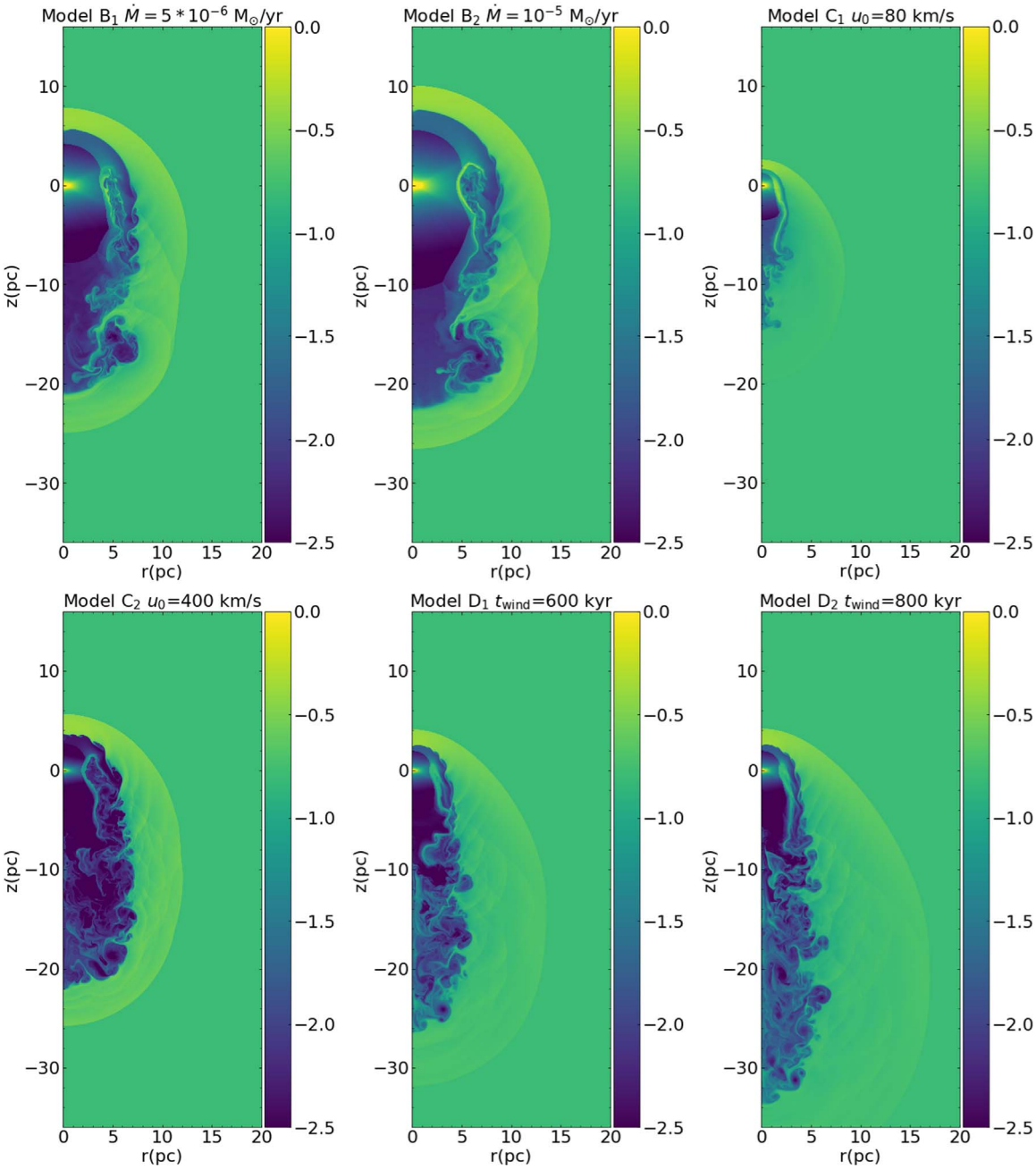

Figure 4. Density maps of the stellar wind for other models (B_1–D_2) in Table 1 at the moment of the SN explosion, respectively. The color bars show the logarithm of density in units of $m_H\,cm^{-3}$.

To sum up, we find that the morphology of the simulated SNR is associated with $\dot{M}$, u_0, and t_{wind}: (1) when employing a higher $\dot{M}$, the shape of the wind-blown bubble is roughly bipolar-like, and the consequent SNR morphology is not comparable to that of the Cygnus Loop; (2) the variations in u_0 could strongly impact the size of the cavity in both directions and increasing t_{wind} gives rise to the elongation of the cavity along the $-z$-direction, both of which could influence the profile of the southern blowout.

3.4. Maps of the Projected SNR

Figures 6 and 7 illustrate the maps of projected SNR at $t_{SNR} = 22$ kyr in the y–z plane for selected models, viewed from

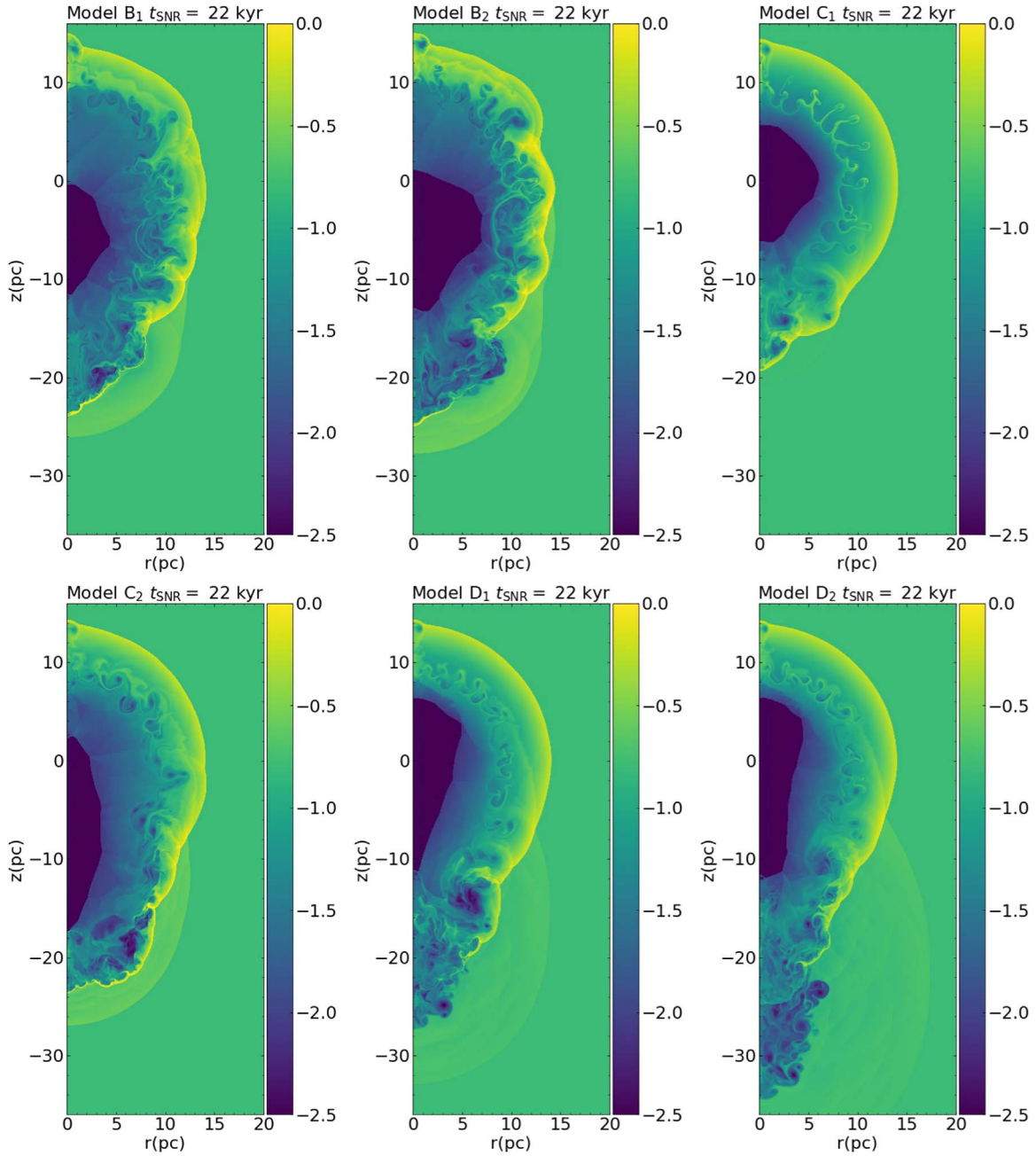

Figure 5. Density profiles of the resulting SNR at $t_{\rm SNR} = 22.0$ kyr for other models (B_1–D_2) in Table 1, respectively. The color bars show the logarithm of density in units of $m_{\rm H}\,{\rm cm}^{-3}$.

four angles relative to the equatorial plane: $\theta_{\rm obs} = 0°$, 15°, 30°, and 45°, respectively. The main results of our simulations are summarized as follows:

Models A, C_2 and D_1. When the observational angle $\theta_{\rm obs}$ varies from 0° to 30°, the northern morphology of the SNR retains a roughly circular shape, while the projected length of the southern blowout along the z-direction decreases with the increasing angle (the projection effect). For $\theta_{\rm obs} = 45°$, the northern profile becomes elliptical, and the longitudinal length of the southern blowout is further reduced. As a result, the overall SNR morphology at $\theta_{\rm obs} = 45°$ deviates from a Cygnus-Loop-like structure. Besides, if $\theta_{\rm obs}$ is $\gtrsim$30°, there will be some prominent stripes and arcs in the northern circular region due to the projection effect. The absence of such features in the observations may imply that $\theta_{\rm obs}$ could not be too large.

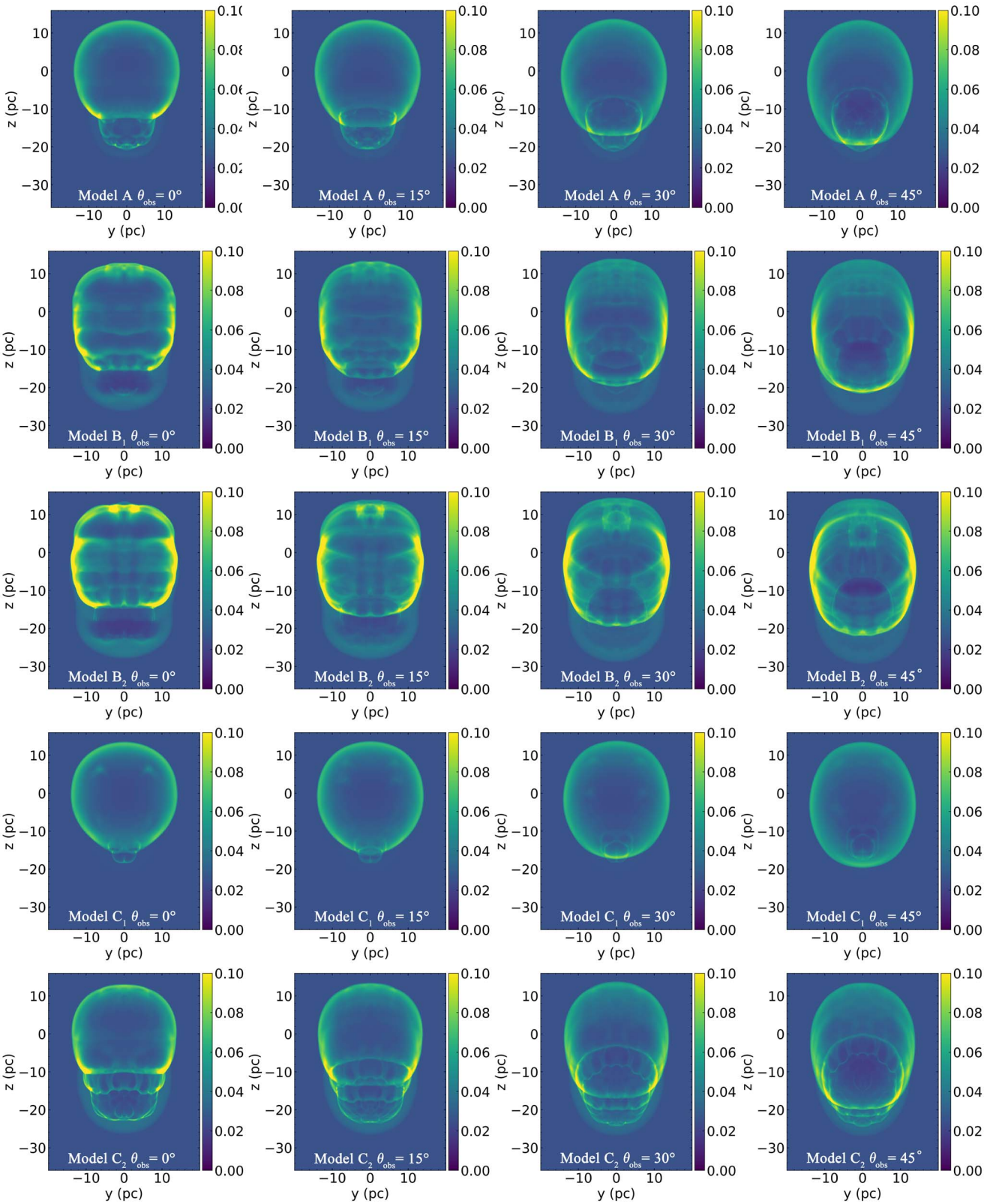

Figure 6. Projection of the square of the SNR density with θ_{obs} in the y–z plane for Models A (top panels), B_1–B_2 (middle top and middle panels), and C_1–C_2 (middle bottom and bottom panels), respectively. The observational angle θ_{obs}, representing the angle between the equatorial plane and the line of sight, is set at 0°, 15°, 30°, and 45°, respectively. The color bars show the intensity scaling in units of m_H^2 cm^{-6}.

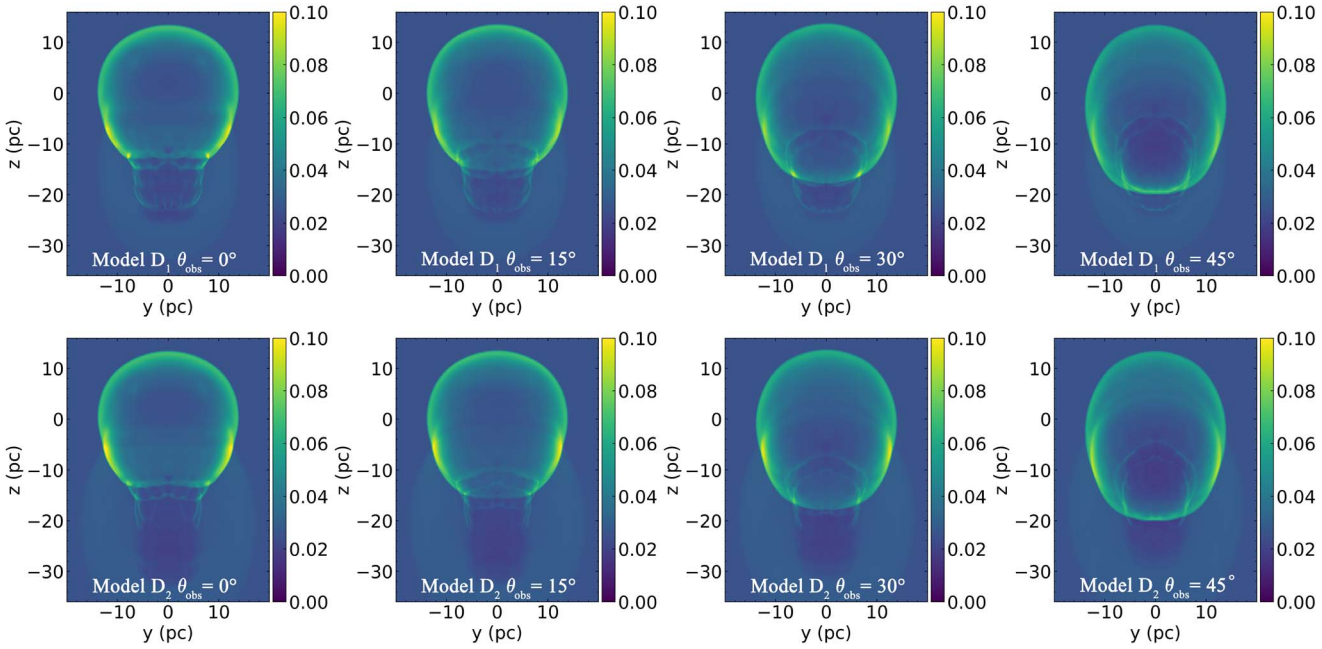

Figure 7. Same as Figure 6, but for Models D_1 (top panels), and D_2 (bottom panels), respectively.

Models B_1 and B_2. For an inclination angle $\theta_{\rm obs} = 0°$, the northern part of projected SNR morphology exhibits a rectangular shape rather than a circular one. The southern outline of FS is not distinct, which is probably due to the low-density in the wind-blown cavity (H. Uchida et al. 2009). In sum, a Cygnus-Loop-like profile could not be reproduced within our Models B_1–B_2 (higher mass-loss rate).

Model C_1. Since the southern blowout at $\theta_{\rm obs} = 0°$ is not manifested, the SNR morphology at other viewing angles could not be Cygnus-Loop-like.

Model D_2. At different $\theta_{\rm obs}$, the overall morphology of the SNR is similar to the results of Model D_1. Because of the further extension of the low-density tunnel along the $-z$-direction, the southernmost FS remains in the low-density region at $t_{\rm SNR} = 22$ kyr, not yet interacting with the cavity boundary, resulting in an indistinct southern outline.

Following the aforementioned procedures for measuring three physical quantities (i.e., $R_{\rm b}$, $\theta_{\rm b}$, and $R_{\rm s}$) of the Cygnus Loop, we extract the same quantities as in Figure 1 from the simulation results to characterize the final SNR morphologies. This could provide a further comparison with the X-ray observations of the Cygnus Loop. Using the observational data from N. A. Levenson et al. (1998, 1999), we obtain $\theta_{\rm b} = 68\overset{\circ}{.}23$ and $R_{\rm b}/R_{\rm s} = 1.39$ for the Cygnus Loop. In Figure 8, we plot $\theta_{\rm b}$ against $R_{\rm b}/R_{\rm s}$ for simulated SNRs from Models A, C_2, and D_1 in Figures 6 and 7, where the southern blowout is apparent at $\theta_{\rm obs} = 0°$. The results of Model A resemble those of Cygnus Loop. With a larger u_0 of 400 km s^{-1} (Model C_2), the results show a large $\theta_{\rm b}$. Additionally, Model D_1 exhibits higher values

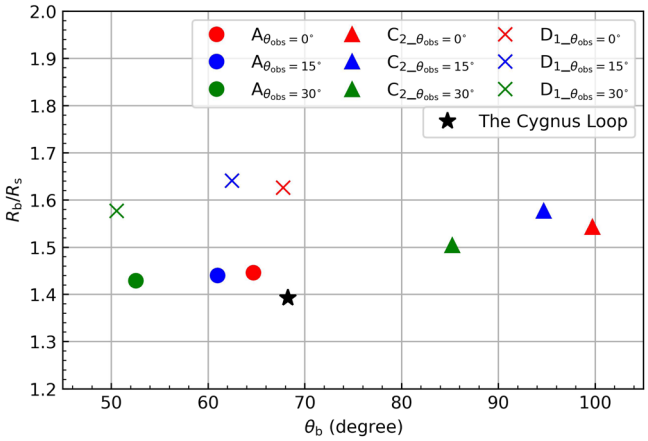

Figure 8. The comparisons of $\theta_{\rm b}$ and $R_{\rm b}/R_{\rm s}$ from models in Figures 6 and 7 with the measurement results of the Cygnus Loop. The dots, triangles, crosses, and star denote the measurement results for Models A, C_2, D_1, and the Cygnus Loop, respectively. "$A_{\theta_{\rm obs}=0°}$" stands for "Model A with $\theta_{\rm obs} = 0°$", while "$C_{2\_\theta_{\rm obs}=15°}$" represents "Model C_2 with $\theta_{\rm obs} = 15°$". Similar notations are applied to the other models. Because the southern blowout is not apparent in Models B_1–B_2, C_1, and D_2, the extractions of $\theta_{\rm b}$ and $R_{\rm b}/R_{\rm s}$ are precluded from these models.

of $R_{\rm b}/R_{\rm s}$ under a long $t_{\rm wind}$ of 600 kyr. These results are qualitatively consistent with the results of 2D simulations in Section 3.3. For the reason mentioned above, we do not extract $\theta_{\rm b}$ and $R_{\rm b}/R_{\rm s}$ from Models B_1–B_2, C_1, and D_2.

Moreover, in Figure 9, $R_{\rm b}/R_{\rm s}$ and $\theta_{\rm b}$ are extracted from the same models in Figure 8 to quantitatively appraise the impact

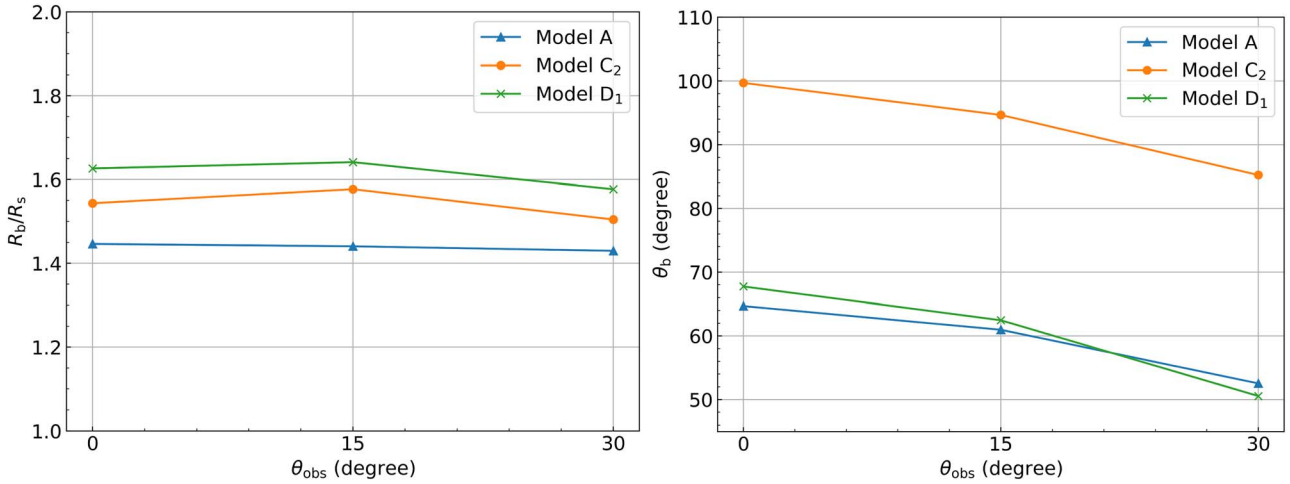

Figure 9. R_b/R_s (left panel) and θ_b (right panel) for Models A, C_2, and D_1 vs. θ_{obs}.

of a varying θ_{obs} on the observed SNR patterns. With regard to R_b/R_s, the ratio is not seriously affected when θ_{obs} varies from 0° to 30°. In contrast, θ_b drops monotonically with an increasing θ_{obs} ($\lesssim$30°). In conclusion, changes in θ_{obs} do indeed affect the geometric characteristics of the projected morphology of simulated SNRs. Under our stellar-wind model, an increase in θ_{obs} ($\lesssim$30°) contributes to a reduction in θ_b, while leaving few impacts on R_b/R_s. However, when θ_{obs} exceeds 45°, the projected morphology of simulated SNR significantly deviates from a Cygnus-Loop-like structure. Therefore, for $\theta_{obs} \lesssim 30°$, a projected morphology akin to the Cygnus Loop could be also synthetized under specific conditions: (1) R_b/R_s of the SNR profile at $\theta_{obs} = 0°$ is close to its counterpart of the Cygnus Loop; and (2) the initial θ_b is slightly larger than the observation. If these two conditions are satisfied, adjusting θ_{obs} within the range of 0°–30° may render the projected SNR more comparable to that of the Cygnus Loop, regarding both the synthetized morphology and the extracted quantities.

4. Discussion and Conclusions

4.1. Discussion

Regarding the numerical simulations for the Cygnus Loop, the bipolar stellar-wind model we impose here could be an alternative to other scenarios proposed by J. Fang et al. (2017) and D. M.-A. Meyer et al. (2020, 2024). In the model of J. Fang et al. (2017), a two-stage anisotropic wind and a runaway progenitor star are proposed. The latitude-dependent stellar winds produce a wind bubble with an irregular limb, then the SN explodes inside the low-density cavity. The FS of the SNR interacts with those wind-blown structures, which reproduces some observed irregular depressions along the limb of the Cygnus Loop in X-rays, such as the bump in the west, a planar from the east to southeast (see Figure 1) (J. J. Hester & D. P. Cox 1986; N. A. Levenson et al. 1998). Concerning the model in D. M.-A. Meyer et al. (2020), a drop-like cavity is formed by a time-dependent multiple-stage isotropic stellar wind emanating from the progenitor. Consequently, an SNR evolves in this circumstellar environment, shaping a profile resembling the appearance of the Cygnus Loop. In D. M.-A. Meyer et al. (2024), due to the stellar proper motion accompanied by a time-dependent isotropic stellar wind, the cavity is elongated along the opposite direction of systemic motion. Thereafter, the interaction between the ejecta and the cavity induces a Cygnus-Loop-like SNR. According to the observations of the RSG stars, we suggest a one-stage bipolar stellar-wind model in Section 2.2, which follows different descriptions and yields SNR profiles comparable to the observations. The interpretation for the blowout formation in our scenario, i.e., the FS moving into a low-density tunnel, is similar as in these studies. The maximum width of the low-density tunnel at $t_{wind} = 400$ kyr presented in Figure 2 is approximately 5 pc, closely aligning with the findings of W. H.-M. Ku et al. (1984).

For all these scenarios, the low-density cavity with a proper shape and size plays an important role in shaping the SNR's morphology, especially the southern blowout. In fact, such a cavity arises from the combined effects of the stellar proper motion and the stellar winds. On the one hand, if the progenitor lacks proper motion, the resulting cavity may not be elongated in a certain direction. On the other hand, without an appropriate stellar wind, the size of the cavity may not be suitable for the formation of an evident blowout. For example, if the progenitor star is stationary, the cavity shaped by stellar wind will be circular. When the stellar wind is equatorial (i.e., the stellar wind material is mainly injected along the *r*-direction), the cavity may either be excessively wide in the *r*-direction (at a

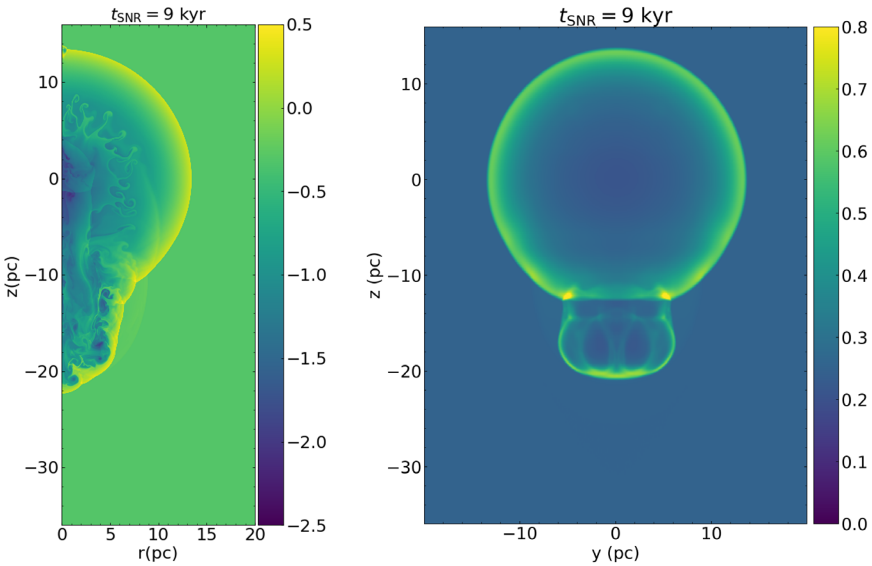

Figure 10. Density profile of the resulting SNR at $t_{SNR} = 9$ kyr in Model A with $E_{ej} = 0.7 \times 10^{51}$ erg and $n_{ISM} = 0.5\,cm^{-3}$ (R. A. Fesen et al. 2018b) (left panel). Projection of the square of the SNR density at $\theta_{obs} = 0°$ in the y–z plane (right panel).

high stellar-wind velocity) or insufficiently long in the $-z$-direction (under a low stellar-wind velocity). Hence, within the numerical framework, a reasonable description for the stellar wind combined with a stellar proper motion is essential in creating a southern cavity of suitable size. In this regard, our bipolar wind model and the isotropic wind model discussed in D. M.-A. Meyer et al. (2020, 2024) are both feasible in reproducing a Cygnus-Loop-like SNR.

Besides, there are differing views on the values of explosion energy E_{ej} and the density of the ISM n_{ISM}, with a deduced E_{ej} ranging from 0.05 to 0.7×10^{51} erg (S. Rappaport et al. 1974; E. Miyata & H. Tsunemi 1999; A. Preite Martinez 2011; R. A. Fesen et al. 2018b), and n_{ISM} from 0.1 to $0.5\,cm^{-3}$ (W. H.-M. Ku et al. 1984; N. A. Levenson et al. 1998; J. Bohigas et al. 1999; J. C. Raymond et al. 2003). In this work, we adopt $E_{ej} = 0.06 \times 10^{51}$ erg and $n_{ISM} = 0.16\,cm^{-3}$. As a supplement to our simulations, we also conduct 2D and 3D runs based on Model A with a larger explosion energy of $E_{ej} = 0.7 \times 10^{51}$ erg and a higher ISM density of $n_{ISM} = 0.5\,cm^{-3}$ (R. A. Fesen et al. 2018b) (see Figure 10). The outcomes show a Cygnus-Loop-like SNR morphology, featuring a nearly circular northern part and a pronounced southern blowout. Such large uncertainties in the physical parameters of the Cygnus Loop (such as E_{ej}, n_{ISM}, and t_{SNR}) indicate that further observations are required for clarification.

4.2. Conclusions

The Cygnus Loop, as observed in X-rays, exhibits a nearly circular limb with an evident blowout in the south. By performing a set of HD simulations in 2D cylindrical and 3D Cartesian coordinate systems, we seek to study the formation mechanism of the peculiar periphery of this specific source. To this end, we have proposed a specific stellar-wind model for an investigation: a bipolar stellar wind descending from a runaway progenitor. Our simulation results suggest that the overall morphology of the Cygnus Loop, along with its southern blowout, may originate from the interactions between the expanding SNR and the preexisting wind-blown structures.

We take Model A as the benchmark case, assuming the progenitor star with a proper motion of $30\,km\,s^{-1}$ and an anisotropic stellar wind governed by Equations (5)–(6). Initially, a bipolar-like low-density cavity evacuated by stellar wind manifests around the star. Owing to stellar proper motion, the cavity elongates along the $-z$-direction during the stellar-wind evolution. Once an SN explodes in such a modified circumstellar environment, the northern FS would sweep over the stellar surroundings and then travel through the unshocked ISM, creating a circular shape. Meanwhile, a portion of the southern FS expands inside the low-density cavity, resulting in the formation of a distinct blowout in the remnant's southern region. At $t_{SNR} = 22$ kyr, the overall simulated periphery of our benchmark SNR (Figure 3) is analogous to its X-ray counterpart of the Cygnus Loop (Figure 1). Furthermore, current observations also support the idea that some SNRs interact with the surrounding wind-blown structures created by their progenitor stars' mass-loss (J. E. Jencson et al. 2016; S. Mandal et al. 2023; D. Dickinson et al. 2024).

Since the morphology of SNR is closely related to the circumstellar structures, we assess the influences on the wind bubble and resulting SNR profiles (see Figures 4 and 5) from different model parameters in Table 1. The outcomes show that

a Cygnus-Loop-like SNR could be reproduced under appropriate parameter combinations. More explicitly, the SNR morphology is affected by the physical characteristics of the wind-blown cavity, such as the overall shape and the size of the low-density tunnel in both directions. These characteristics could be seriously altered by the stellar-wind parameters of the progenitor star (i.e., the mass-loss rate $\dot{M}$, stellar-wind velocity u_0, and integration time for wind $t_{\rm wind}$).

The major conclusions drawn from 2D simulations are summarized below: (1) regarding high mass-loss rates ($5\times10^{-6}\,M_\odot\,{\rm yr}^{-1}$ and $10^{-5}\,M_\odot\,{\rm yr}^{-1}$), we find that the cavity reveals a roughly bipolar morphology at $t_{\rm wind}=400\,{\rm kyr}$. As a result, the profile of our final SNR deviates from the shape of the Cygnus Loop; (2) the stellar wind possessing a low u_0 ($80\,{\rm km\,s}^{-1}$) could only generate a small-sized wind bubble around the progenitor star, thereby hindering the formation of a southern blowout. If we adopt a large u_0 ($400\,{\rm km\,s}^{-1}$), the cavity will be elongated along both directions during the wind evolution. Therefore, an over-sized blowout is produced by the subsequent SN explosion; and (3) with a long integration time $t_{\rm wind}$ (600 kyr and 800 kyr), the cavity would further evolve in the south and thus influence the profile of the blowout.

Lastly, we produce the morphology of projected SNR in Figures 6 and 7, namely the projection of the square of the SNR density from four observational angles to the equatorial plane: $\theta_{\rm obs}=0°$, 15°, 30°, and 45°. In Figure 8, $\theta_{\rm b}$ (the central angle of the blowout) and $R_{\rm b}/R_{\rm s}$ (the distance from the northern center to the southernmost point of the blowout divided by the average radius of the northern shock limb) are extracted from models and compared with their counterparts of the Cygnus Loop. Among these models, we find that the results of Model A are the most adjacent to their counterparts of the Cygnus Loop. However, the method employed to determine these three physical quantities ($R_{\rm b}$, $R_{\rm s}$, and $\theta_{\rm b}$) might introduce some errors, as the circle may not be the most appropriate one to fit the general limb of the northern FS in the figures. Considering Figure 9, our results imply that, the viewing angle could affect the projected SNR morphology, notably the southern blowout. In our stellar-wind model, for $\theta_{\rm obs}\lesssim30°$, a Cygnus-Loop-like SNR could be also synthetized under specific conditions: (1) $R_{\rm b}/R_{\rm s}$ of the SNR profile at $\theta_{\rm obs}=0°$ is close to its counterpart of the Cygnus Loop; and (2) the initial $\theta_{\rm b}$ is slightly larger than the observation. If the two conditions are met, adjusting $\theta_{\rm obs}$ within the range of 0°–30° may give rise to a projected SNR more comparable to that of the Cygnus Loop, regarding both the synthetized morphology and the extracted quantities.

The nature of the Cygnus Loop's origin has been debated a lot (P. A. Charles et al. 1985; H. Uchida et al. 2009; R. A. Fesen et al. 2018b). In addition to the stellar-wind scenario, an alternative scenario, in which the Cygnus Loop expands in a low-density region surrounded by molecular clouds of different densities (R. A. Fesen et al. 2018b), has been proposed and is worth further examining. Additionally, apart from the shock-cavity interactions, some other mechanisms would also vary the profile of an SNR. For example, the ejecta clumps near the CD and the back-reaction of accelerated cosmic rays can enhance the growth of RTI and shrink the separation between the FS and the CD respectively, modifying the morphological evolution of SNRs (G. Ferrand et al. 2010; S. Orlando et al. 2012). This, together with the shock-cavity interactions, might all be attributed to the formation of those irregular depressions on the edge of the Cygnus Loop. Accordingly, further investigations, with regard to the molecular clouds scenario as well as some realistic physical processes occurring during the evolution, will provide a more comprehensive description of the specific origin of the Cygnus Loop.

Acknowledgments

This work is partially supported by the National Natural Science Foundation of China (NSFC, 12233006). B.W.B. is partially supported by the NSFC 12203042, and the Foundations of Yunnan Province 202301AU070009. The numerical computations were conducted on the Yunnan University Astronomy Supercomputer.

References

Aschenbach, B., & Leahy, D. A. 1999, A&A, 341, 602
Asida, S. M., & Tuchman, Y. 1995, ApJ, 455, 286
Balick, B., & Frank, A. 2002, ARA&A, 40, 439
Bandiera, R. 1987, ApJ, 319, 885
Beasor, E. R., Davies, B., Smith, N., et al. 2020, MNRAS, 492, 5994
Blondin, J. M., & Ellison, D. C. 2001, ApJ, 560, 244
Blondin, J. M., & Lundqvist, P. 1993, ApJ, 405, 337
Blondin, J. M., Lundqvist, P., & Chevalier, R. A. 1996, ApJ, 472, 257
Bohigas, J., Sauvageot, J. L., & Decourchelle, A. 1999, ApJ, 518, 324
Brandner, W., Grebel, E. K., Chu, Y.-H., & Weis, K. 1997, ApJL, 475, L45
Braun, R., & Strom, R. G. 1986, A&A, 164, 208
Cassam-Chenaï, G., Decourchelle, A., Ballet, J., et al. 2004, A&A, 414, 545
Castor, J., McCray, R., & Weaver, R. 1975, ApJ, 200, 107
Charles, P. A., Kahn, S. M., & McKee, C. F. 1985, ApJ, 295, 456
Chevalier, R. 1982, ApJ, 258, 790
Chiotellis, A., Boumis, P., & Spetsieri, Z. T. 2020, Galax, 8, 38
Chiotellis, A., Schure, K. M., & Vink, J. 2012, A&A, 537, A139
Das, S., Brose, R., Meyer, D. M. A., et al. 2022, A&A, 661, A128
Davies, B. 2017, RSPTA, 375, 20160270
Davies, B., Oudmaijer, R. D., & Sahu, K. C. 2007, ApJ, 671, 2059
De Marco, O. 2009, PASP, 121, 316
Dickinson, D., Smith, N., Andrews, J. E., et al. 2024, MNRAS, 527, 7767
Dwarkadas, V. V. 2005, ApJ, 630, 892
Dwarkadas, V. V., Chevalier, R. A., & Blondin, J. M. 1996, ApJ, 457, 773
Fang, J., Yu, H., & Zhang, L. 2017, MNRAS, 464, 940
Ferrand, G., Decourchelle, A., Ballet, J., et al. 2010, A&A, 509, L10
Fesen, R. A., Neustadt, J. M., Black, C. S., & Milisavljevic, D. 2018a, MNRAS, 475, 3996
Fesen, R. A., Weil, K. E., Cisneros, I., Blair, W. P., & Raymond, J. C. 2021, MNRAS, 507, 244
Fesen, R. A., Weil, K. E., Cisneros, I. A., Blair, W. P., & Raymond, J. C. 2018b, MNRAS, 481, 1786
García-Segura, G. 1997, ApJ, 489, L189
García-Segura, G., & López, J. A. 2000, ApJ, 544, 336
García-Segura, G., López, J. A., & Franco, J. 2005, ApJ, 618, 919
Hester, J. J., & Cox, D. P. 1986, ApJ, 300, 675
Jencson, J. E., Prieto, J. L., Kochanek, C. S., et al. 2016, MNRAS, 456, 2622

Jun, B.-I., & Jones, T. W. 1999, ApJ, 511, 774
Katsuda, S., Takiwaki, T., Tominaga, N., Moriya, T. J., & Nakamura, K. 2018, ApJ, 863, 127
Kirshner, R. P., & Taylor, K. 1976, ApJ, 208, L83
Ku, W. H.-M., Kahn, S. M., Pisarski, R., & Long, K. S. 1984, ApJ, 278, 615
Lee, J.-J., Koo, B.-C., Snell, R. L., et al. 2012, ApJ, 749, 34
Levenson, N. A., Graham, J. R., Aschenbach, B., et al. 1997, ApJ, 484, 304
Levenson, N. A., Graham, J. R., Keller, L. D., & Richter, M. J. 1998, ApJS, 118, 541
Levenson, N. A., Graham, J. R., & Snowden, S. L. 1999, ApJ, 526, 874
Levesque, E. M. 2010, NewAR, 54, 1
Mandal, S., Duffell, P. C., Polin, A., & Milisavljevic, D. 2023, ApJ, 956, 130
Massey, P., & Olsen, K. A. G. 2003, AJ, 126, 2867
McCray, R., & Snow, T. P. J. 1979, ARA&A, 17, 213
Meyer, D. M.-A., Langer, N., Mackey, J., Velázquez, P. F., & Gusdorf, A. 2015, MNRAS, 450, 3080
Meyer, D. M.-A., Mignone, A., Petrov, M., et al. 2021a, MNRAS, 506, 5170
Meyer, D. M.-A., Petrov, M., & Pohl, M. 2020, MNRAS, 493, 3548
Meyer, D. M.-A., Pohl, M., Petrov, M., & Oskinova, L. 2021b, MNRAS, 502, 5340
Meyer, D. M.-A., Velázquez, P. F., Pohl, M., et al. 2024, A&A, 687, A127
Mignone, A., Bodo, G., Massaglia, S., et al. 2007, ApJS, 170, 228
Mignone, A., Zanni, C., Tzeferacos, P., et al. 2012, ApJS, 198, 7
Minkowski, R. 1958, RvMP, 30, 1048
Miyata, E., & Tsunemi, H. 1999, ApJ, 525, 305
Miyata, E., Tsunemi, H., Kohmura, T., Suzuki, S., & Kumagai, S. 1998, PASJ, 50, 257
Miyata, E., Tsunemi, H., Pisarski, R., & Kissel, S. E. 1994, PASJ, 46, 101
Muller, S., Dinh-V-Trung Lim, J., Hirano, N., Muthu, C., & Kwok, S. 2007, ApJ, 656, 1109
Orlando, S., Bocchino, F., Miceli, M., Petruk, O., & Pumo, M. L. 2012, ApJ, 749, 156
Preite Martinez, A. 2011, A&A, 527, A55
Rappaport, S., Doxsey, R., Solinger, A., & Borken, R. 1974, ApJ, 194, 329
Raymond, J. C., Ghavamian, P., Sankrit, R., Blair, W. P., & Curiel, S. 2003, ApJ, 584, 770
Reynolds, S. P., Borkowski, K. J., Hwang, U., et al. 2007, ApJ, 668, L135
Seok, J. Y., Koo, B. C., Zhao, G., & Raymond, J. C. 2020, ApJ, 893, 79
Seward, F. D. 1990, ApJS, 73, 781
Shull, P., Jr, & Hippelein, H. 1991, ApJ, 383, 714
Sun, X. H., Gao, X. Y., Reich, W., et al. 2022, RAA, 22, 125011
Sun, X. H., Reich, W., Han, J. L., Reich, P., & Wielebinski, R. 2006, A&A, 447, 937
Hekkert, P., Chapman, J. M., & Zijlstra, A. A. 1992, ApJ, 390, L23
Tenorio-Tagle, G., Bodenheimer, P., Franco, J., & Rozyczka, M. 1990, MNRAS, 244, 563
Tenorio-Tagle, G., Rozyczka, M., Franco, J., & Bodenheimer, P. 1991, MNRAS, 251, 318
Uchida, H., Tsunemi, H., Katsuda, S., & Kimura, M. 2008, ApJ, 688, 1102
Uchida, H., Tsunemi, H., Katsuda, S., et al. 2009, ApJ, 705, 1152
Uyanıker, B., Reich, W., Yar, A., Kothes, R., & Fürst, E. 2002, A&A, 389, L61
Velázquez, P. F., Meyer, D. M. A., Chiotellis, A., et al. 2023, MNRAS, 519, 5358
Vink, J. 2012, A&AR, 20, 49
Weaver, R., McCray, R., Castor, J., Shapiro, P., & Moore, R. 1977, ApJ, 218, 377
Williams, B. J., Blair, W. P., Blondin, J. M., et al. 2011, ApJ, 741, 96
Zhekov, S. A., & Myasnikov, A. V. 2000, ApJ, 543, L53
Zhou, Y. 2017a, PhR, 720, 1
Zhou, Y. 2017b, PhR, 723, 1